Quantification of sub-resolution porosity in carbonate rocks by applying high-salinity contrast brine using X-ray microtomography differential imaging

Qingyang Lin[1,*], Yousef Al-Khulaifi[1], Martin J. Blunt[1], Branko Bijeljic[1]

[1]*Department of Earth Science and Engineering, Imperial College London, London, SW7 2AZ, United Kingdom*

**Corresponding author:*

Tel.: +44 2075949982.

E-mail address: q.lin11@imperial.ac.uk (Q. Lin)

Address: Department of Earth Science and Engineering, Imperial College London, London, SW7 2AZ, United Kingdom

Keywords: Carbonate, X-ray microtomography, sub-resolution porosity, micro-porosity, differential imaging

Key Highlights

1) A new flow-based method quantifies sub-resolution porosity in carbonates.
2) Good agreement between porosity from image analysis and Helium measurement.
3) Connectivity is provided and distribution of sub-resolution porosity is evaluated.

Abstract

Characterisation of the pore space in carbonate reservoirs and aquifers is of utmost importance in a number of applications such as enhanced oil recovery, geological carbon storage and contaminant transport. We present a new experimental methodology that uses high-salinity contrast brine and differential imaging acquired by X-ray tomography to non-invasively obtain three-dimensional spatially resolved information on porosity and connectivity of two rock samples, Portland and Estaillades limestones, including sub-resolution micro-porosity. We demonstrate that by injecting 30 wt% KI brine solution, a sufficiently high phase contrast can be achieved allowing accurate three-phase segmentation based on differential imaging. This results in spatially resolved maps of the solid grain phase, sub-resolution micro-pores within the grains, and macro-pores. The total porosity values from the three-phase segmentation for two carbonate rock samples are shown to be in good agreement with Helium porosity measurements. Furthermore, our flow-based method allows for an accurate estimate of pore connectivity and a distribution of porosity within the sub-resolution pores.

1. Introduction

Carbonate rocks are important geological porous media which are associated with many applications including hydrocarbon recovery [1], carbon storage [2] and contaminant transport [3]. Estimates show that carbonate reservoirs hold more than half of the world's hydrocarbon reserves [4]. They are known to have a very complex pore space whose structure and connectivity, dependent on the processes studied, have a significant impact on single and multiphase flow, and transport and reactive properties [5-10]. Therefore, the main goal of our study is to obtain a full characterisation of the pore space, which hitherto has not been fully resolved.

Anovitz et al. [11] have reviewed different methods for measuring porosity, including direct measurements such as Helium (He) porosimetry and Mercury Intrusion Capillary Pressure (MICP) measurements, as well as imaging methods and techniques such as Optical Petrology, Scanning Electron Microscopy (SEM) and Nuclear Magnetic Resonance (NMR) imaging. However, although some direct measurement methods can yield accurate porosity values, it is challenging to resolve all the pore space, particularly sub-micron porosity. Two-dimensional methods may have higher resolution, but they do not show how the pore spaces are connected. Hence, having a technique which can provide spatially-resolved three-dimensional (3D) porosity values is important for both experimental and simulation studies.

X-ray microtomography (also called XMT or micro-CT) and image processing has been widely used in geologically-related studies [12-18], and in recent years this technique has been applied in visualisation of multiphase flow and reactive transport in geological porous media [19-24]. However, one of the main limitations of this method is the limited spatial resolution, which is typically of order of 1 μm or larger [22]. High resolution images (e.g. tens of nano meters voxel size by nano CT) may be obtained, but for a smaller samples (e.g. tens of microns sample size) that may not capture the full range of pore sizes in a representative elementary volume. In theory, the grey-scale of the grains could be used to estimate the intra-granular porosity, but this assumes a uniform mineralogy and complete connection of all the sub-resolution porosity. To illustrate this, we provide example XMT images for our Portland and Estaillades carbonate cores in Figure 1. The XMT measured porosity, based on the larger pores only, is much lower than the porosity obtained by Helium porosimetry, as presented later. There is a range of grey scales for the grains, but as we will show, this alone does not quantify the extent of connected sub-resolution pores.

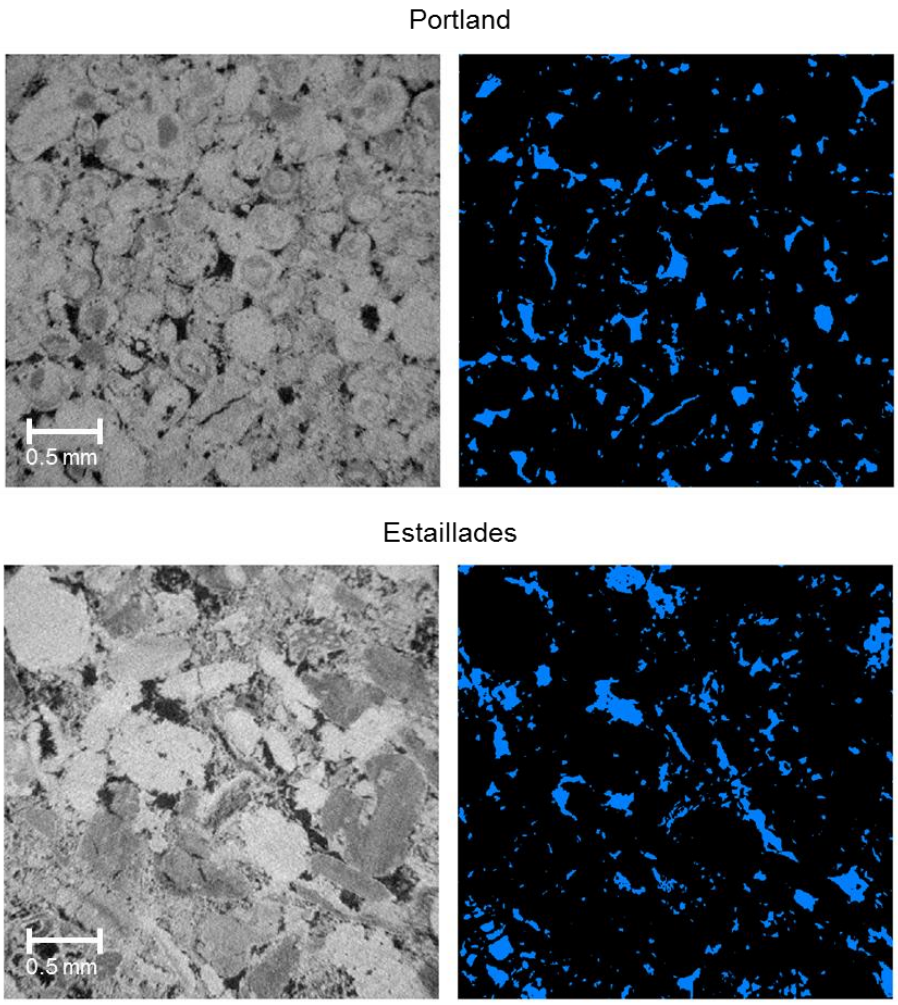

Figure 1. Example two-dimensional slices of a three-dimension image (with dimensional of 650^3 voxels at voxel size of 5 µm) for the Portland and Estaillades samples. The grey-scale image is shown on the left and the segmented image on the right. The porosity of the segmented image is 0.078 for Portland and 0.130 for Estaillades; this contrasts with Helium (He) porosity values of 0.195±0.006 and 0.293±0.007 respectively (conducted at Imperial College London, UK).

Sub-resolution porosity is one of the main parameters required for a full description of flow and reactive transport processes in porous media, such as determination of permeability and dynamics of dissolution-precipitation mechanisms using the XMT imaging technique[25-27]. Combining XMT images and local two-dimensional Scanning Electron Microscopy (SEM) images was shown to be able to resolve sub-resolution pores [28, 29]. However, the main limitations for fully utilising SEM images are that they require extensive time and effort to acquire. In most cases, only part of the sample is imaged, while at the same time pore-space connectivity of sub-resolution pore space is not confirmed from the experiment, as in the flow based methods. In some studies, segmenting sub-resolution pores directly from dry scans has been attempted by assuming that grains with an intermediate grey-scale were regions with sub-resolution pores [25, 30-34]. However, most of the porosity values measured from image analysis cannot be matched with the porosity values obtained by other methods. Freire-Gormaly et al. [35] studied the sensitivity of different thresholding techniques to segment the pore space, including sub-resolution pores for carbonates, applied to Indiana Limestone and Pink Dolomite. They showed that a single imaging technique and

thresholding method cannot alone determine porosity from a dry scan only. The main problem for segmenting sub-resolution pores from dry scan is, as we present below, that a grain with an intermediate grey-scale may have sub-resolution pores, or simply be composed of a different mineralogy, or contain pores that are not connected to the macro-pore space. Thresholding a dry scan alone cannot distinguish between these cases. Moreover, some of the main issues such as connectivity of the sub-resolution pores could not be addressed.

One of the potential solutions is to introduce a new material phase to provide better image contrast for sub-resolution pores. Boone et al. [36] performed a differential imaging experiment in Massangis limestone comparing dry scans with scans obtained once the rock sample was saturated with 5% CsCl to account for the contribution of sub-resolution pores to the total porosity values. However, their results were not close to the porosity obtained by MICP measurements. Ghous et al. [37] used a mixture of di-iodomethane (CH_2I_2) and toluene as the contrast phase to resolve sub-resolution porosity, but their experimental method requires a reference scan for pure air and a pure reference material such as calcite and cannot be easily applied in conjunction with a flow experiment. Latham et al. [38] studied registration algorithms to align the dry scan image and the image with a contrast fluid (1M CsI). Bhattad et al. [39] introduced a flow-based method using 1M NaI-H_2O solution to quantify sub-resolution pores within laminated sandstones. Pini [40] introduced a method to quantify porosity by imaging gas absorption between two gas phases using a medical CT scanner. However, the resolution in this study is approximately one millimetre.

Differential imaging technique is currently one of the most promising methods to resolve sub-resolution porosity. However, new experimental procedures and image processing methods need to be developed to enhance the phase contrast. In this paper, a general experimental and image acquisition procedure is designed by utilising differential imaging that non-invasively provides porosity and connectivity of sub-resolution pores for two exemple carbonate rocks, Portland and Estaillades. Based on difference images, three phase segmentation is used to segment grain phases, sub-resolution pore phase and macro pore phase. Porosity values for the sub-resolution pore phase are quantified and a method is presented to estimate pore connectivity by a distribution of porosity within the sub-resolution pores. The total porosity values from three phase segmentation are shown to be in good agreement with Helium porosity measurements.

2. Experimental methodology

2.1 Rock Samples

The rock samples we used in this study are Portland and Estaillades limestones. We selected these two carbonates as they contain a large volume of porosity below a typical voxel size from XMT. This is seen in Figure 2 that shows the pore size distribution for these two rocks [41] measured by the MICP method (conducted at Weatherford Laboratories, East Grinstead, UK) on cores of bulk volume 6.778 cm^3 for Portland and 6.792 cm^3 for Estaillades from the same blocks from which our

XMT imaged samples were drilled from. According to Figure 2, there are more than 50% of the pores in both carbonates below the 5 µm voxel size (a voxel size we used for XMT imaging). In addition, both samples contain grains with and without sub-resolution pores.

In order to compare them with the XMT imaging results in later sections, the porosity values for the cores used in differential imaging experiment were measured with Helium porosimetry (conducted at Imperial College London, UK), from which the values of 0.195±0.006 for Portland and 0.293±0.007 for Estaillades were obtained. Here the bulk volume is 0.182 cm^3. The uncertainty quoted is one standard deviation in the instrument error.

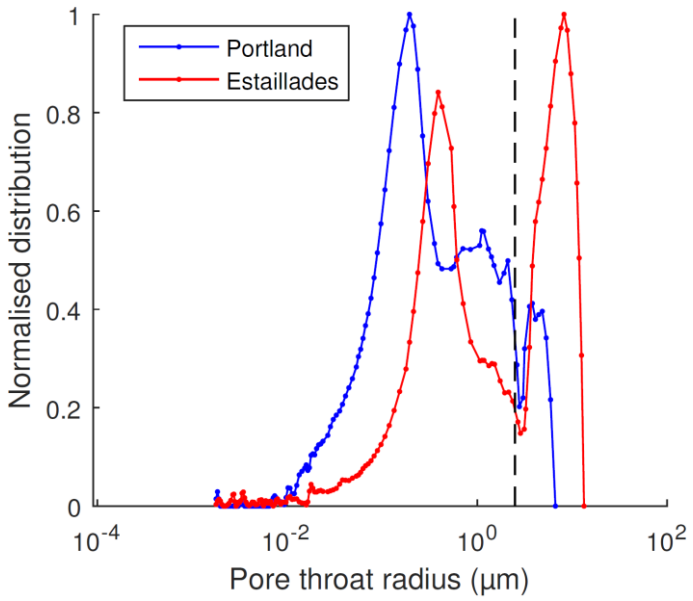

Figure 2. Pore throat radius distribution of Portland and Estaillades samples obtained from MICP measurements on the Portland core (6.778 cm^3 bulk volume) and Estaillades core (6.792 cm^3 bulk volume) [41]. The total porosities for these Portland and Estaillades cores were 0.200 and 0.302 respectively from Helium (He) measurements. The vertical dashed line at 2.5 µm marks half of the voxel size of 5 µm used in our XMT experiments.

2.2 Experimental methodology

The experimental apparatus is shown in Figure 3. The XMT samples were drilled into cylindrical cores 4.81 mm in diameter and 10.0 mm in length. The cores were then placed into a fluoro-polymer elastomer (Viton) sleeve, which was attached to metal fittings (end piece) connecting the core to the pore-fluid flowlines. This assembly was then placed within a Hassler-type flow cell. Detailed information about the flow cell can be found in Andrew et al. [19]. High pressure syringe pumps were used to maintain pressure and control flow in the pore-space of the rock.

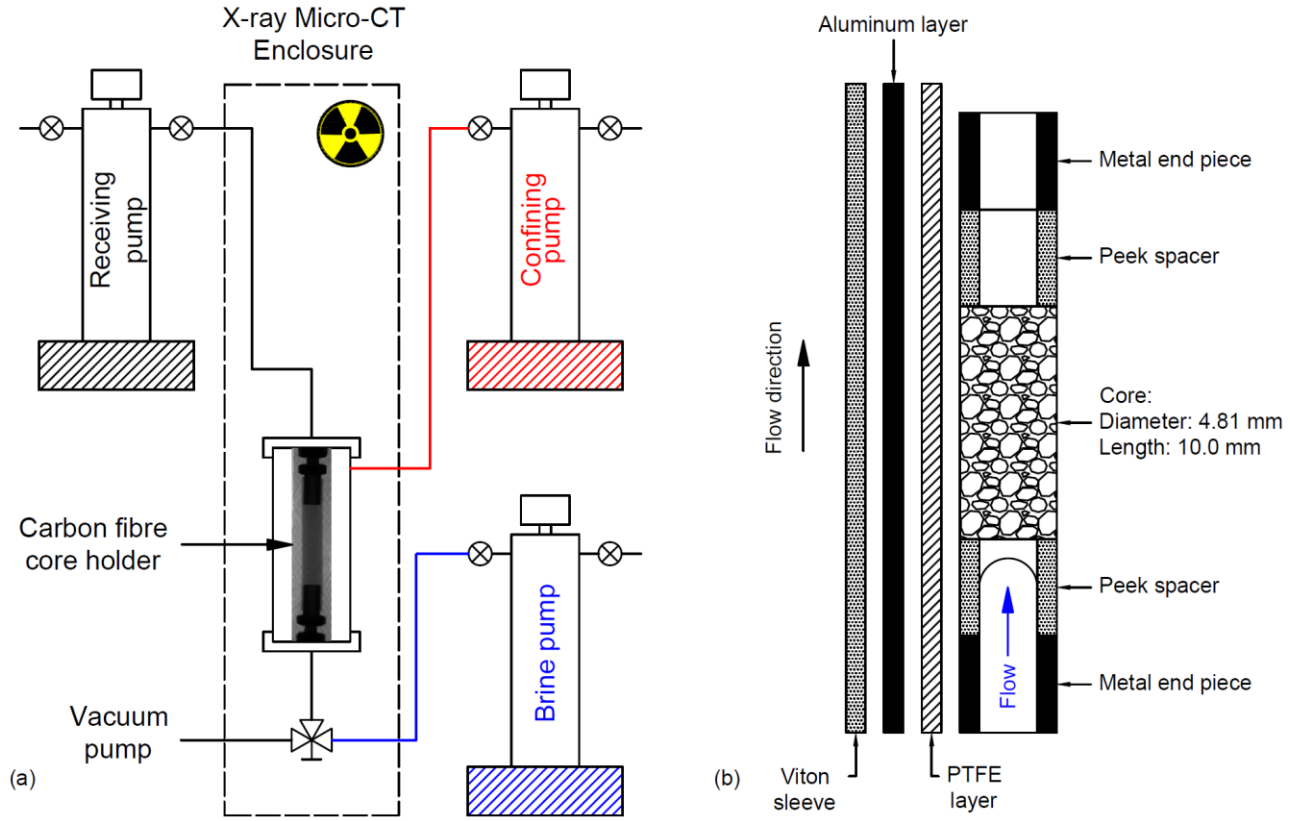

Figure 3. Experimental apparatus. (a) The pump system to control flow. (b) Details of the core assembly.

The brine solution was made from deionised water with a prescribed amount of Potassium Iodide (KI). KI was used as an ionic salt as it has a high atomic weight causing a high X-ray attenuation coefficient, allowing it to be used as a contrast agent. The salinity of the brine was designed to have three values, namely 5 wt%, 10 wt% and 30 wt%. By having different concentrations of KI the image contrast quality can be compared. The brine injected from the brine pump at different concentrations was initially pre-equilibrated with the host rock to prevent fluid/solid chemical reaction.

Each experiment was conducted using the following procedure:

1. A confining pressure of 3 MPa (30 bar) was applied and maintained within the cell to compress the Viton sleeve around the core sample to avoid any fluid bypass.
2. A dry (air) scan was taken at room temperature.
3. Before injection, the system was vacuumed to ensure full saturation after brine injection.
4. More than 1000 pore volumes of KI doped (5 wt%) brine were injected from the brine pump at a low flow rate (1 ml/min) for more than 1 hour through the core sample to ensure full saturation.
5. After 100% brine saturation was achieved, a brine saturated scan was taken.
6. Steps 4 and 5 were then repeated but with 10 wt% and then 30 wt% KI.

The imaging was performed using a Versa XRM-500 X-Ray Microscope. To optimise the image quality, each sample at different KI concentration was scanned with 80 keV at a voxel size of 5 µm. The three-dimensional images were reconstructed from a set of 2001 projections by using the Avizo software on the Versa system. After reconstruction all the images were registered (aligned) according to the reference dry (air) scan – this was done in order to have the same orientation and position for visualisation and comparison. The images used in later sections are cropped cubic sections with a dimension of 650^3 voxels: this represents a bulk volume of 0.034 cm^3, or approximately one fifth of the total sample size.

3. Results and discussion

Our main goal is to segment sub-resolution porosity accurately, and to assign values for porosity in sub-resolution regions. The reconstructed images for brine saturated Portland and Estaillades samples at different KI concentrations are shown in Section 3.1. Differential imaging results showing the difference between brine saturated scan and dry scan are compared in Section 3.2, where it can be observed that the highest KI concentration (30 wt%) provides the best phase contrast and image quality. The solid grain phase, sub-resolution pore phase and macro pore phase are segmented using both global thresholding and a modified watershed segmentation method in Section 3.3. The average porosity values for the sub-resolution pore phases for both samples are assigned to the segmented label images (Section 3.4) and the overall sample porosity measured by XMT imaging is compared with Helium porosimetry measurements (Section 3.5). The connectivity of the sub-resolution pores and macro pores, as well as the distribution of sub-resolution pores are then provided and discussed in Section 3.6.

3.1 Reconstructed images

Figure 4 and Figure 5 show the same slice from the raw image for both Portland and Estaillades samples respectively at different KI concentrations. The grey regions in the dry (air) scan are potential regions with sub-resolution pores. With the highest brine concentration (30 wt% in this study), the brine absorbs X-rays more strongly than the solid, and hence brine-saturated regions appear bright in the image. The regions highlighted by the white boxes show grains that remain the same shade of grey – these are more likely to be solid grains with low density minerals, or at least those with disconnected sub-resolution pores – while grains that become lighter contain connected sub-resolution pores which can be accessed by KI doped brine.

Regions 1 and 2 for Portland shown in Figure 4 illustrate the identification of sub-resolution porosity. From a dry scan, these regions might be considered as grains containing sub-resolution pores as the voxel grey-scale values (CT numbers) are quite close to the values for macro pores. However, after 30 wt% KI doped brine invasion, many of these regions remain a similar shade of grey, as shown in Figure 4d. These regions are therefore interpreted as comprising minerals with a low density or containing pore space that is not accessible to brine, and hence are considered as solid phase, or at least unconnected void space. Comparing with the methods which segment sub-

resolution pores directly from dry scans, using high concentration KI doped brine as a contrast phase can avoid the misidentification of low density minerals as sub-resolution connected pores.

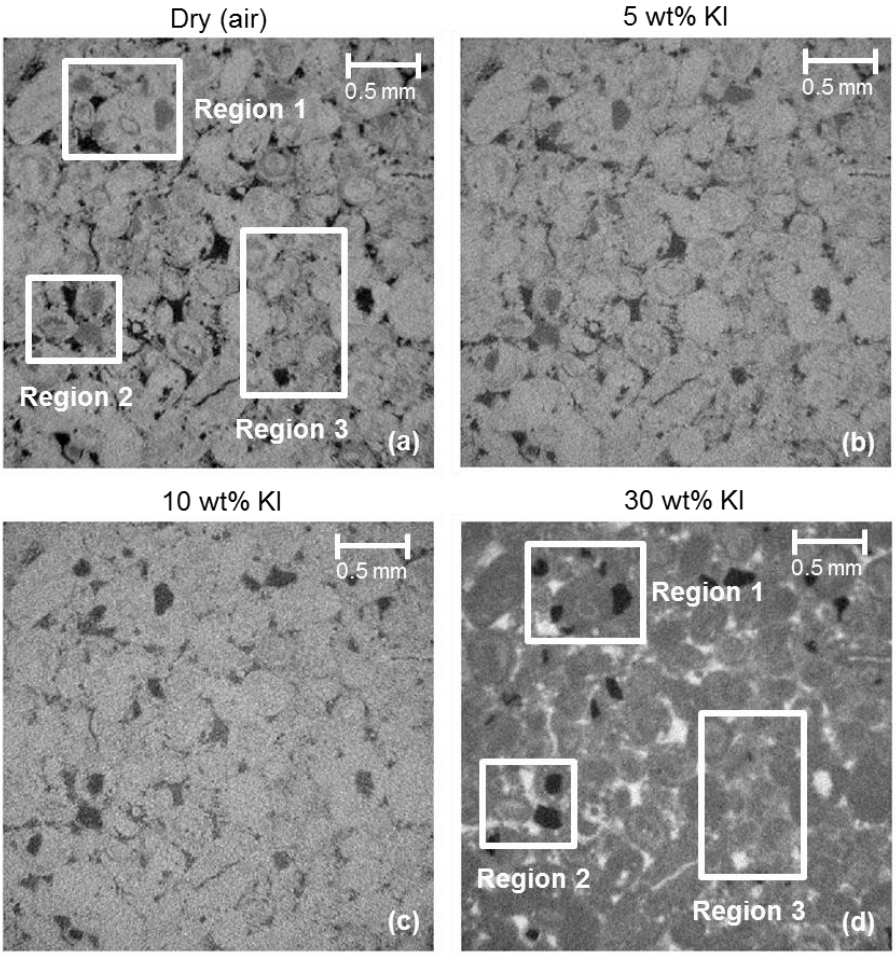

Figure 4. An example reconstructed XMT slice of Portland with different KI concentrations: (a) Dry (air) scan. (b) Sample saturated with 5 wt% KI doped brine. (c) Sample saturated with 10 wt% KI doped brine. (d) Sample saturated with 30 wt% KI doped brine: here the brine is the lightest phase. The boxes shown in the dry scan indicate the example regions 1, 2 and 3 with potential sub-resolution pores. The areas that remain a similar shade of grey are solid grains with low density minerals, while the regions that become lighter contain connected sub-resolution porosity.

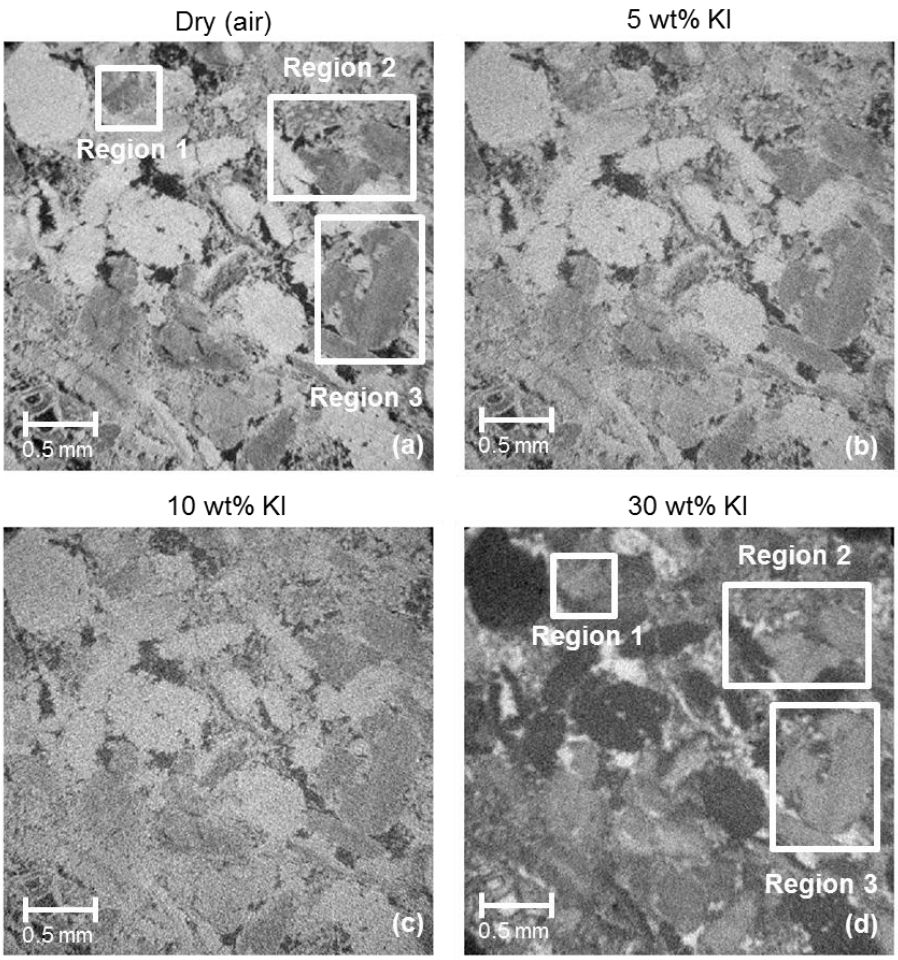

Figure 5. An example reconstructed XMT slice of Estaillades showing the same slice with different KI concentration: (a) Dry (air) scan. (b) Sample saturated with 5 wt% KI doped brine. (c) Sample saturated with 10 wt% KI doped brine. (d) Sample saturated with 30 wt% KI doped brine. As in Figure 4 the boxes highlight regions with both solid grains (remaining the same shade) and sub-resolution porosity (which becomes lighter).

3.2 Differential images

The differential image between the KI saturated scan and the dry scan can maximise the phase contrast between grain phase and pore phase. The differential image between the KI saturated scan and the dry (air) scan can be obtained from:

$$\mathrm{CT(differential)} = \mathrm{CT(KI\ saturated\ scan)} - \mathrm{CT(Dry\ scan)} + \mathrm{CT0} \qquad (1)$$

where CT is the CT number of each voxel and CT0 is some large positive constant (65535 in this example) to avoid negative values. The resultant images are shown in Figure 6 and Figure 7. In the histograms for the differential images, lower grey-scale values towards the left hand side of the histogram are solid grain phase (including disconnected pores), the higher grey-scale values towards the right hand side are the macro pore phase, and intermediate values in the middle are the sub-resolution pore phase.

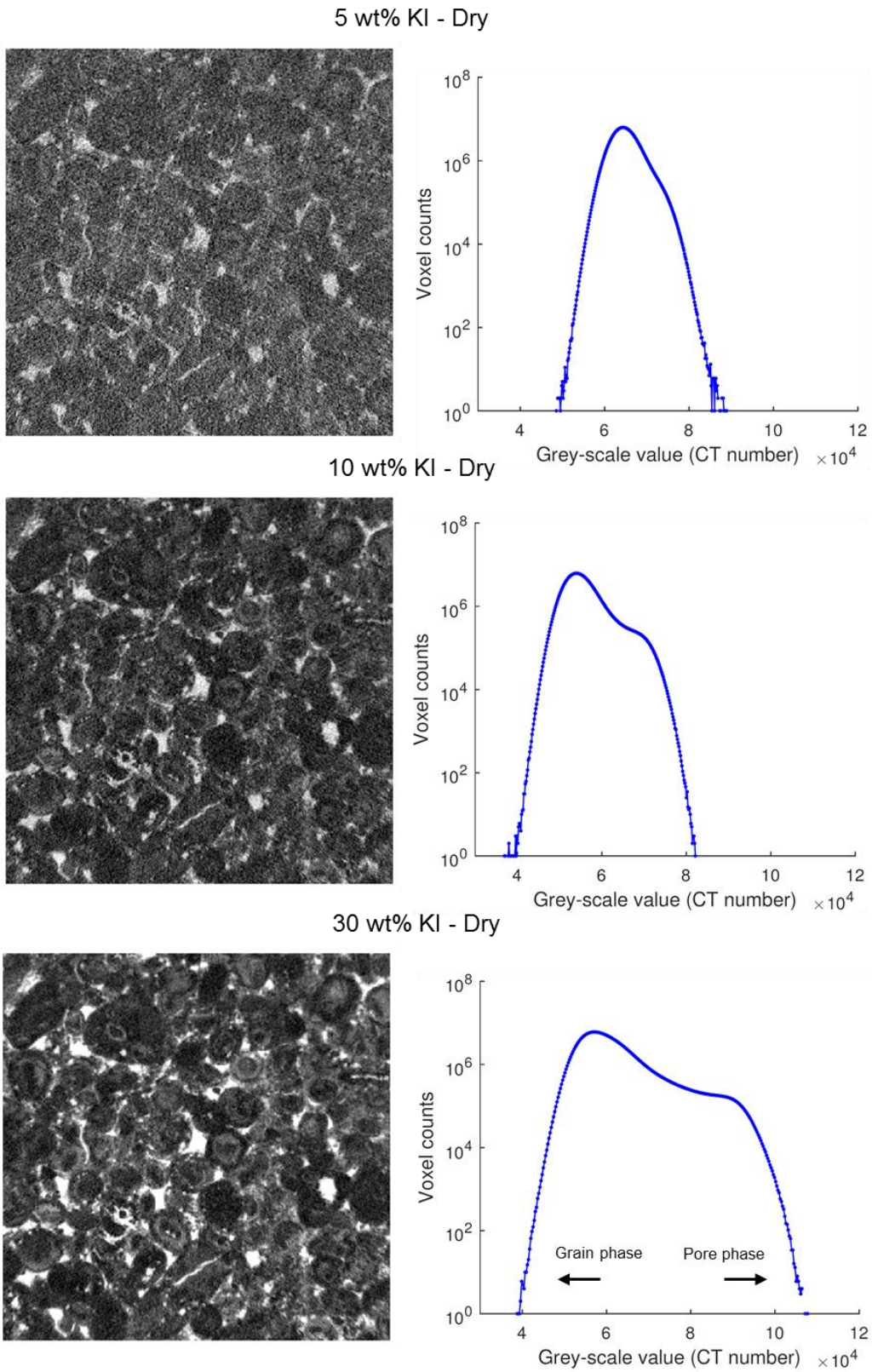

Figure 6. The difference in grey-scale values between the KI saturated scans at different concentrations and the dry scan for Portland. The histograms for the three images at different KI concentrations are plotted showing that the data range within the histogram is much wider at the highest KI concentration, which indicates that the sub-resolution pores are more distinguishable. The voxels with lower grey-scale value are the solid grain phase while the voxels with higher grey-scale values are the pore phase. The two-dimensional slices also show that three phases including solid grain phase (dark), sub-resolution pores (intermediate grey) and macro pores (bright) can be distinguished; the highest phase contrast and image quality can be observed in the differential image at 30 wt% KI.

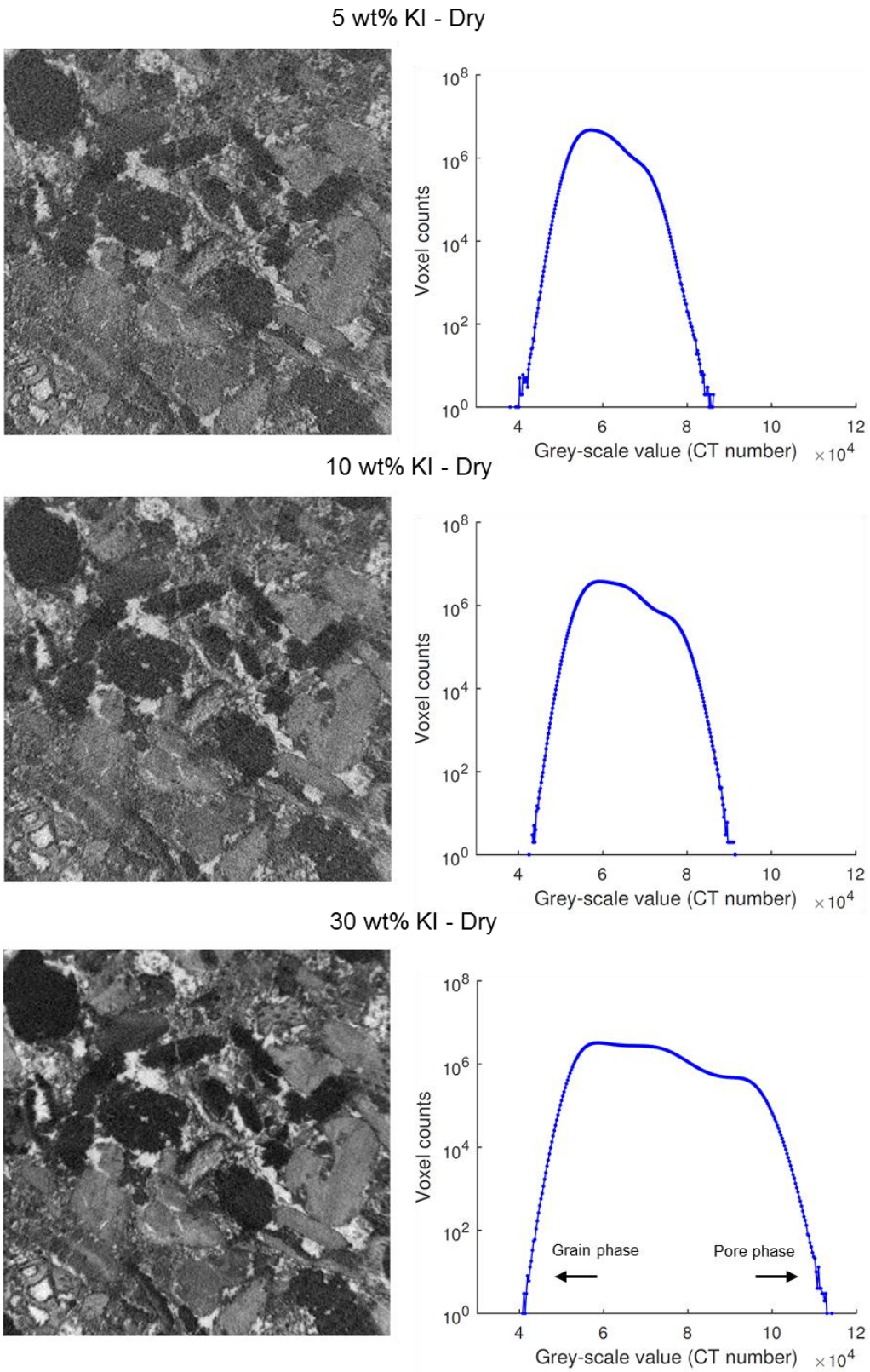

Figure 7. The difference in grey-scale values between the KI saturated scans at different concentrations and the dry scan for Estaillades. The histograms for the three images at different KI concentrations are plotted showing that the data range within the histogram is much wider at the highest KI concentration, which indicates that the sub-resolution pores are more distinguishable. The voxels with lower grey-scale value are the solid grain phase while the voxels with higher grey-scale values are the pore phase. The two-dimensional slices also show that three phases including solid grain phase (dark), sub-resolution pores (intermediate grey) and macro pores (bright) can be distinguished; the highest phase contrast and image quality can be observed in the differential image at 30 wt% KI.

A key feature of applying differential images is that the solid grain phase with low density minerals can be eliminated to avoid misidentification. For example, in the Portland sample, the regions with low density minerals shown in Figure 4a have low grey-scale values in Figure 6; these will be identified as the solid grain phase.

The differential images with 30 wt% KI concentration show the best image quality and three phases (dark black for grain, grey for sub-resolution pores and white for macro pores) can be distinguished. The main reason for this behaviour is that by using a high concentration KI solution, the phase contrast between pores and grains can be maximised, which is evident by the wider data range in the differential image histograms for both Portland and Estaillades. This makes it possible to perform better segmentation of sub-resolution pores with intermediate grey-scale values between solid grain and pore phase. However, the concentration of KI needs to be maintained below a certain level such that the density of the KI is not too high, which may introduce image artefacts. In later sections, the KI saturated images and the corresponding differential images at 30 wt% concentration are used in segmentation and quantification.

3.3 Three-phase segmentation resolving sub-resolution porosity

3.3.1 Global thresholding based on histogram

The differential images at 30 wt% KI concentration allow the histogram range to be maximised. Three-phase segmentation can be performed based on these differential images. Before segmentation, a non-local means edge preserving filter [42] was applied to reduce the image noise (Figure 8c for Portland and Figure 9c for Estaillades). The filtered differential images were then processed with global thresholding to identify solid grain phase, sub-resolution phase and macro pore phase. The resultant three-phase segmented label images for Portland and Estaillades are shown in Figure 8d and Figure 9d respectively. The parameters (thresholding values shown as red dashed lines) separating the three phases for both samples are shown in Figure 8e and Figure 9e. These parameters are generated using a multi-level Otsu algorithm [43, 44], which maximises the between-class variance of voxel intensity to perform segmentation.

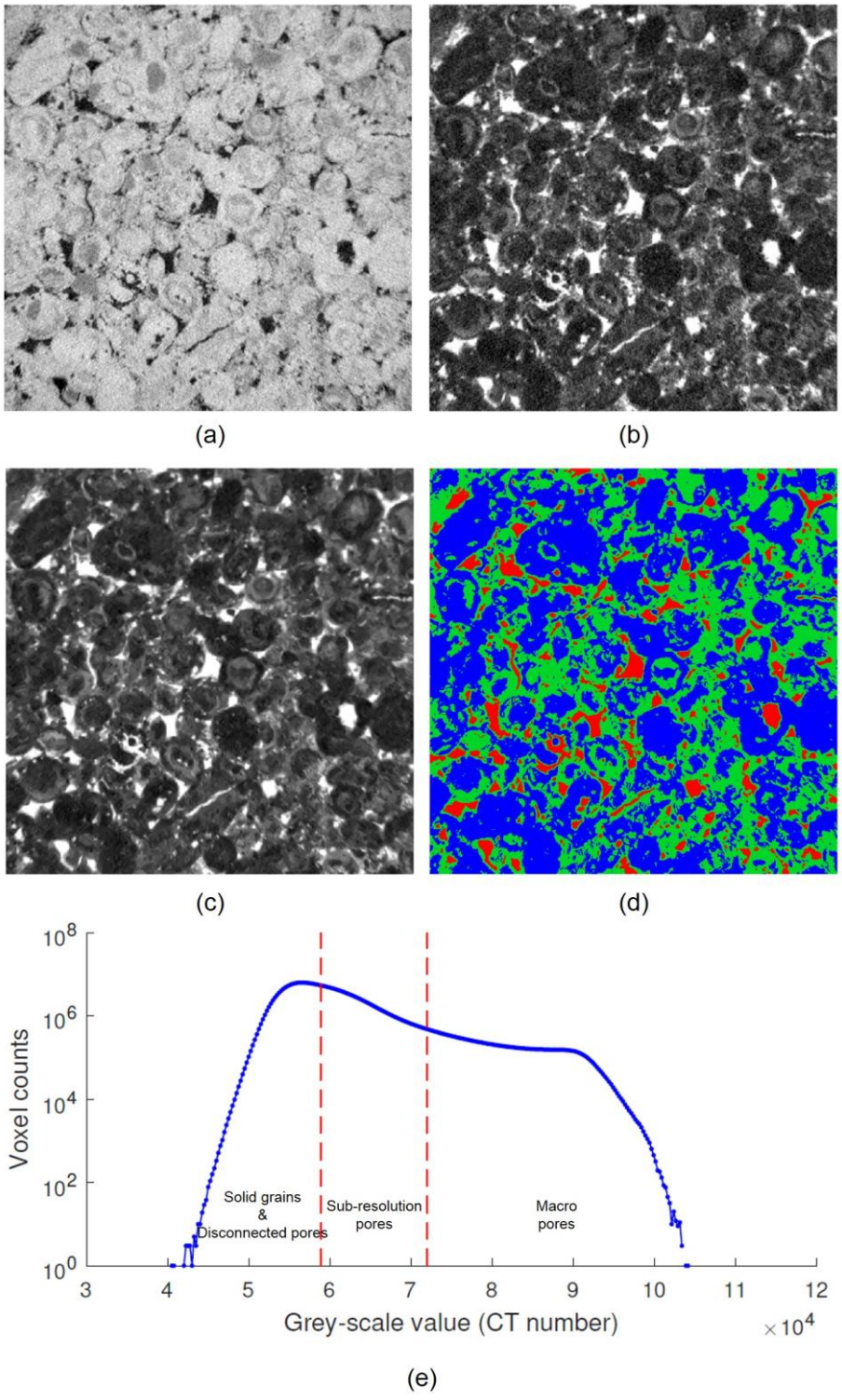

Figure 8. Three-phase segmentation including sub-resolution pores for Portland: (a) An example slice from the original dry scan. (b) The same slice showing the difference in grey-scale values between the KI saturated scan at 30 wt% and the dry scan. (c) The difference image after applying a non-local means edge oreserving filter. (d) Three-phase segmentation showing grains and disconnected pores (blue), sub-resolution pores (green) and macro pores (red). (e) The histogram plot for (d) with thresholding values (red dashed lines) separating three phases. (For interpretation of the references to colour in this figure legend, the reader is referred to the web version of this article.)

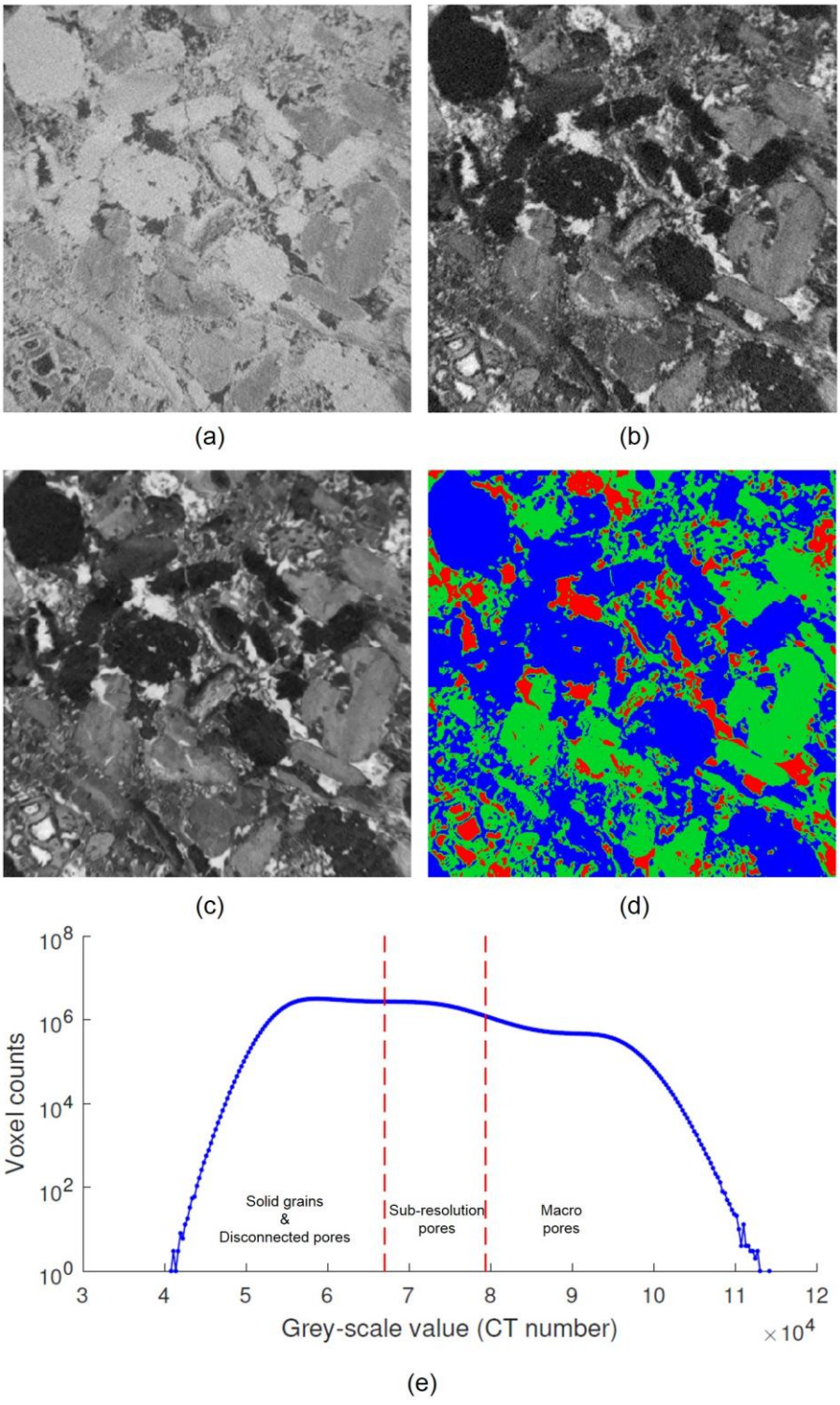

Figure 9. Three-phase segmentation including sub-resolution pores for Estaillades: (a) An example slice from the original dry scan. (b) The same slice showing the difference in grey-scale values between the KI saturated scan at 30 wt% and the dry scan. (c) The difference image after applying a non-local means edge preserving filter. (d) Three-phase segmentation showing grains and disconnected pores (blue), sub-resolution pores (green) and macro pores (red). (e) The histogram plot for (d) with thresholding values (red dashed lines) separating three phases. (For interpretation of the references to colour in this figure legend, the reader is referred to the web version of this article.)

It can be observed that the range for the sub-resolution pore phase for both samples (which is indicated by the distance between two dashed lines in Figure 8e and Figure 9e) are quite similar.

The difference between them is that in the histogram for Estaillades, the sub-resolution pore region is comparatively shifted more to the right which implies that the grains with sub-resolution pores in Estaillades are more porous than those in Portland, as more doped brine can access these regions.

3.3.2 Segmentation using a two-step watershed algorithm

It has been reported that by doing simple histogram based segmentation, arbitrary voxel misidentification may exist, especially at the boundary between two phases, and this can affect the accuracy of segmentation. In order to alleviate this problem, a marker based watershed algorithm which computes off a seed that is generated using a 2D histogram has been developed and applied [19, 23, 45, 46]. The watershed algorithm is normally performed based on a gradient map and it can give accurate segmentation when identifying macro pores from solid grains (see an example shown in [19]). However, as the grey-scale value for the sub-resolution pores are intermediate values, the segmentation becomes more difficult. A two-step marker based watershed segmentation was performed to identify the three phases by segmenting solid grain phase in the first step and macro pores in the second step (Illustrated in Figure 10). The Estaillades sample is used to demonstrate as an example. In the first step, sub-resolution pore phase and macro pore phase were considered as a single phase (the computed seed image is shown in Figure 10b), the solid grain phase was then identified using watershed segmentation. Similarly in the second step, macro pore phase was identified by considering sub-resolution pore phase and solid grains phase as a single phase (the computed seed image is shown in Figure 10c). After identifying the solid grain phase and the macro pore phase, the segmented label for all three phases, shown in Figure 10d, can be generated. The three-phase segmentation using two-step watershed algorithm for Portland is also shown in Figure 11.

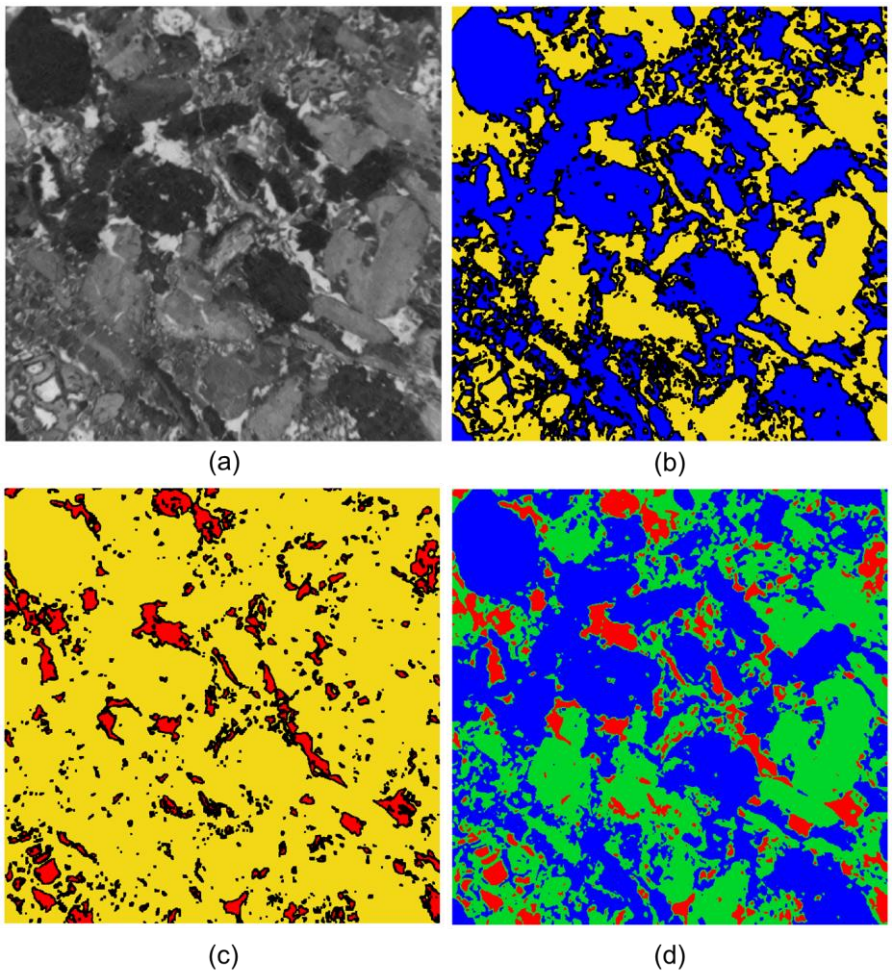

Figure 10. Illustration of the two-step watershed segmentation for Estaillades to identify three phases: (a) An example slice from the differential image (30 wt% KI) after image filtering. (b) The computed seeds for the solid grain phase and the other phases (sub-resolution phase and macro pore phase, shown in yellow). The black region is the region where the boundary between the two phases is calculated by the watershed algorithm. (c) The computed seeds for the macro pore phase and the other phases (sub-resolution phase and solid grain phase, shown in yellow). (d) Three-phase segmented label image showing grain (blue), sub-resolution pores (green) and macro pores (red). (For interpretation of the references to colour in this figure legend, the reader is referred to the web version of this article.)

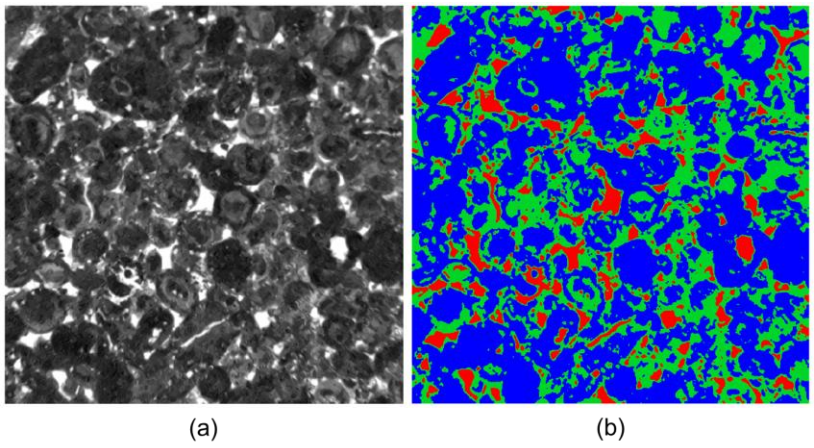

Figure 11. Three-phase segmentation for Portland sample: (a) An example slice from the differential image (30 wt% KI) after image filtering. (b) Three-phase segmented label image showing grain (blue), sub-resolution pores (green) and macro pores (red). (For interpretation of the references to colour in this figure legend, the reader is referred to the web version of this article.)

Figure 12 shows the comparison between segmented label images done by histogram based global thresholding and two-step watershed segmentation. A region of interest (185 x 185 pixels) was used. It can be observed that both methods give reasonably consistent segmentation. However, as the example regions shown in the white boxes indicate, there are some potential misidentifications when using the global thresholding method comparing with the KI saturated scan (the white boxes in Figure 12 highlight regions where voxels more likely to be grain phase were identified as being sub-resolution pore phase). Moreover, there are more isolated voxels which belong to the sub-resolution pore phase when using global thresholding for both samples.

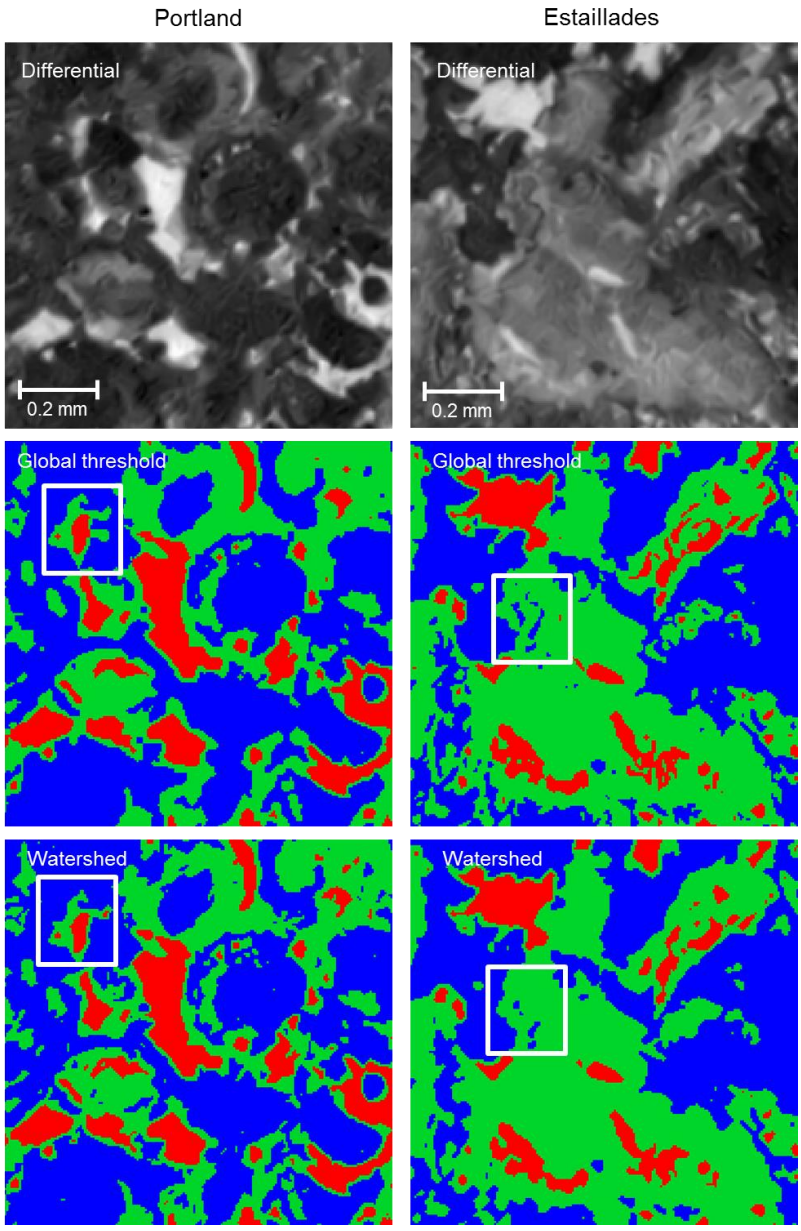

Figure 12. Comparison of segmented label images (solid grain phase is shown in blue, sub-resolution pore phase is shown in green, and macro pore phase is shown in red) for Portland and Estaillades between histogram based global thresholding and two-step watershed segmentation. The results show a region of interest with the dimension of 185 x 185 pixels. The regions in the white boxes are where potential misidentification occurs when using global thresholding. (For interpretation of the references to colour in this figure legend, the reader is referred to the web version of this article.)

3.4 Assigning porosity values to sub-resolution porosity

The average porosity values for the regions with sub-resolution pores can then be quantified by using the segmented label images and the 30 wt% KI saturated images in Figure 4d and Figure 5d (note that no differential images are used for this purpose; KI saturated images are used instead). By using the segmented label images as masks, the histograms for the grey-scale voxels in the KI saturated images can be plotted for each phase. The grey-scale values where the peak values are located for each phase in the histogram are denoted as CT_{grain} for the solid grain phase, CT_{sub} for the sub-resolution pore phase, and CT_{macro} for the macro pore phase. In the KI saturated images, by assuming that the porosity for the grain phase ($\tilde{\phi}_{grain}$) is 0 and the average porosity values for the macro pore phase ($\tilde{\phi}_{macro}$) is 1, the average porosity values within the sub-resolution pore phase ($\tilde{\phi}_{sub}$) for both samples can be obtained by:

$$\tilde{\phi}_{sub} = \left(\frac{\tilde{\phi}_{macro} - \tilde{\phi}_{grain}}{CT_{macro} - CT_{grain}}\right)\left(CT_{sub} - CT_{grain}\right) = \frac{CT_{sub} - CT_{grain}}{CT_{macro} - CT_{grain}} \qquad (2)$$

When comparing the segmented label images using both segmentation methods (Figure 8d and Figure 11b for Portland, Figure 9b and Figure 10d for Estaillades), the main differences occur at the boundaries between phases. The grey-scale values for the voxels located in this region have intermediate values and therefore will not affect the values of CT_{grain}, CT_{sub} *and* CT_{macro} where the peak values exist in the histogram. Thus, the value of $\tilde{\phi}_{sub}$ is very similar when using either global thresholding or the two-step watershed segmentation method: the average values of $\tilde{\phi}_{sub}$ for Portland and Estaillades are 0.294 and 0.436 respectively. This is seen from the histogram and the average porosity values for each phase in both samples using the global thresholding method, as shown in Figure 13.

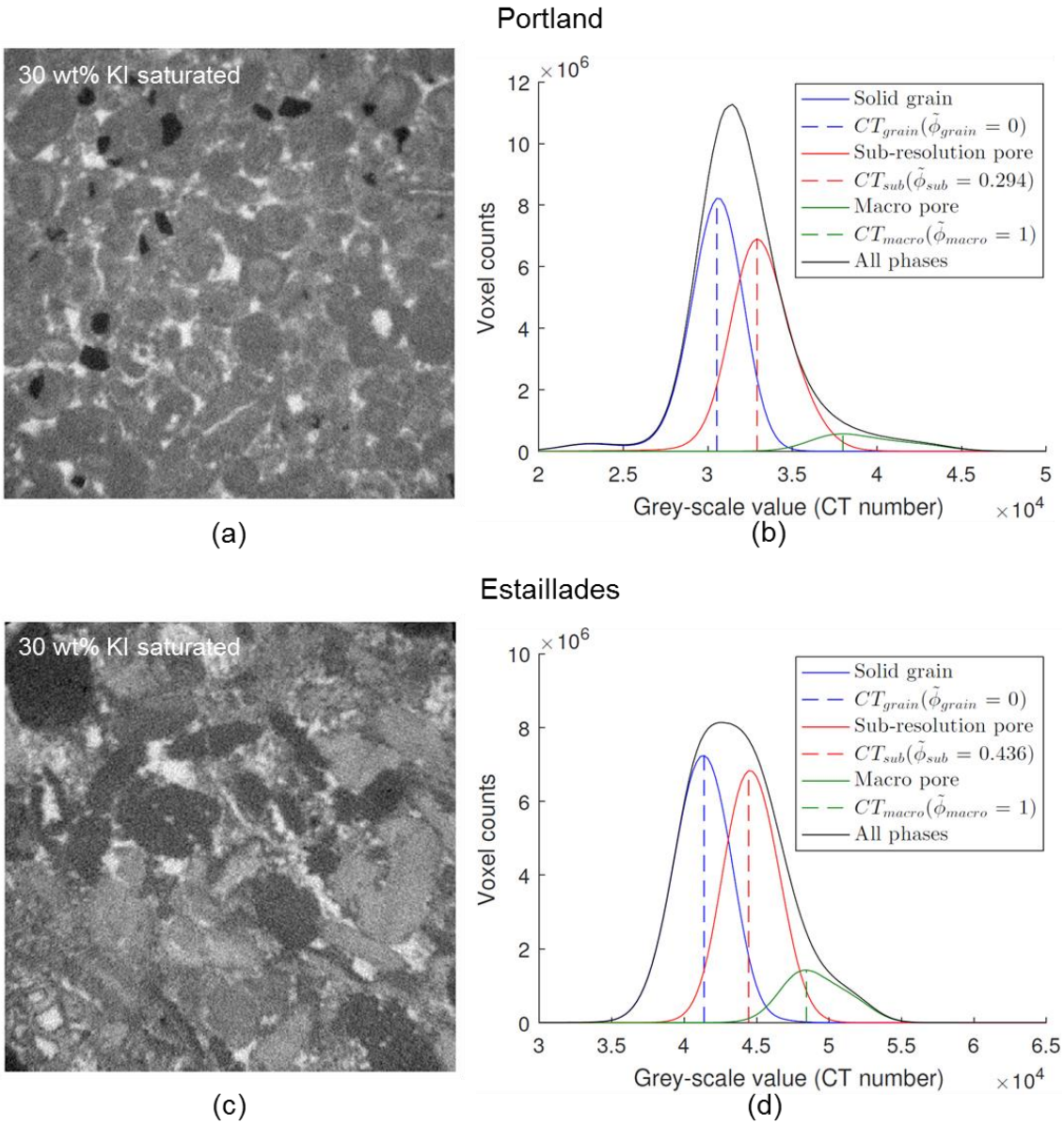

Figure 13. (a) A slice of 30 wt% KI saturated images for Portland. (b) The histograms for the three phases in the KI saturated scan for Portland are plotted based on the segmented label images using a global thresholding method. The dashed lines in the histograms indicate the grey-scale values where the peaks for each phase exist. The porosity values $\tilde{\phi}_{sub}$ for each phase are also assigned. (c) A slice of 30 wt% KI saturated images for Estaillades. (d) The histograms for the three phases in the KI saturated scan for Estaillades.

3.5 Comparison between XMT measurements and Helium porosity measurements

The total porosity (excluding disconnected pores) of the sample (ϕ_{total}) can be described as the sum of porosity contributed by the three phases:

$$\phi_{total} = \phi_{grain} + \phi_{sub} + \phi_{macro} \quad (3)$$

where ϕ_{grain}, ϕ_{sub} and ϕ_{macro} can be expressed as:

$$\phi_{grain} = \tilde{\phi}_{grain} V_{grain} = 0 \quad (4)$$

$$\phi_{sub} = \tilde{\phi}_{sub} V_{sub} \quad (5)$$

$$\phi_{macro} = \tilde{\phi}_{macro} V_{macro} = V_{macro} \quad (6)$$

where the value of $\tilde{\phi}_{grain}$ is 0, the value of $\tilde{\phi}_{macro}$ is 1 and the value of $\tilde{\phi}_{sub}$ is 0.294 for Portland and 0.436 for Estaillades. V_{grain}, V_{sub} and V_{macro} are the total volume fraction for each phase which can be obtained from the segmented label images. The total porosity of the two samples (ϕ_{total}) are shown in Table 1. The results are also compared with Helium porosity measurements on the entire sample.

Table 1. Porosity calculated based on three-phase segmentation from image measurement for Portland and Estaillades compared with the porosity measured by the Helium porosimetry method.

	Portland		**Estaillades**	
	Global thresholding	**Watershed**	**Global thresholding**	**Watershed**
XMT porosity (ϕ_{total})*	0.189	0.193	0.298	0.288
ϕ_{macro}	0.078	0.086	0.130	0.124
ϕ_{sub}	0.111	0.107	0.168	0.164
Helium (He) Porosity	0.195±0.006	0.195±0.006	0.293±0.007	0.293±0.007

It can be seen that the porosity values based on the three-phase segmentation for Portland and Estaillades samples are in good agreement with Helium porosity measurements on the whole core, which has approximately five times the volume of the central section of the rock analysed here. As the sub-resolution porosity is below the XMT resolution, segmentation and the value of $\tilde{\phi}_{sub}$ cannot be perfectly accurate. Our new experimental method and image analysis procedure gives a good estimate of porosity in the sub-resolution region. What is more, since the method is based on a flow experiment, it ignores disconnected porosity, which does not contribute to flow and transport.

3.6 Connectivity

One of the main barriers for simulating fluid flow directly from XMT images is the connectivity of the pore structure, which is limited by the image resolution. If the sub-resolution pore region cannot be resolved, only the macro pore phase is considered. However, the connectivity of macro pores may considerably increase as in fact many of them may be connected through sub-resolution pores.

Figure 14 shows the three-dimensional macro pore structure and the relevant connected macro pore structure with/without considering sub-resolution pores for both samples based on Figure 8d and Figure 9d. Without considering sub-resolution pores, 53.6% of the macro pores are connected for Portland and 84.7% for Estaillades. By allowing macro pores to be connected through sub-

resolution pores, 99.9% and 99.7% of macro pores are connected in Portland and Estaillades respectively. These values are expected to be close to 100% since brine can access both macro pore and sub-resolution pore regions in our flow-based experiments (as shown in the KI saturated scans, Figure 6 and Figure 7).

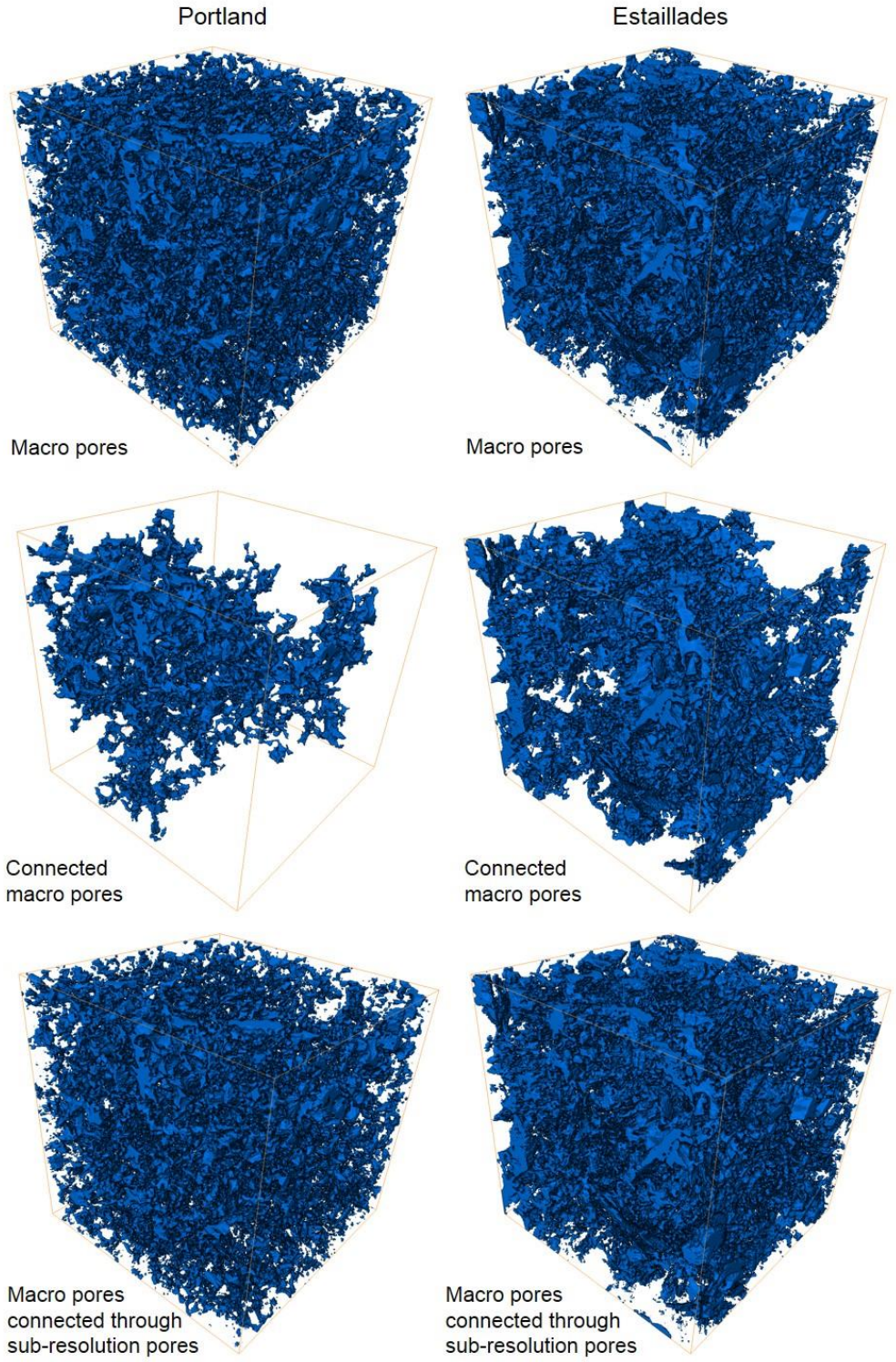

Figure 14. Three-dimensional visualisation of the macro pore structure, connected macro pores structure and connected macro pore structure through sub-resolution pores for Portland and. The volumes of connected macro pores without considering sub-resolution pores are significantly reduced.

In Figure 15 we illustrate how macro pores in Portland are connected through sub-resolution micro pores. The connectivity increases both for the macro pores between the grains (Cases 1 and 2 in Figure 15) but can also be enhanced where the macro pores exist closer to the grain centres (Case 3 in Figure 15).

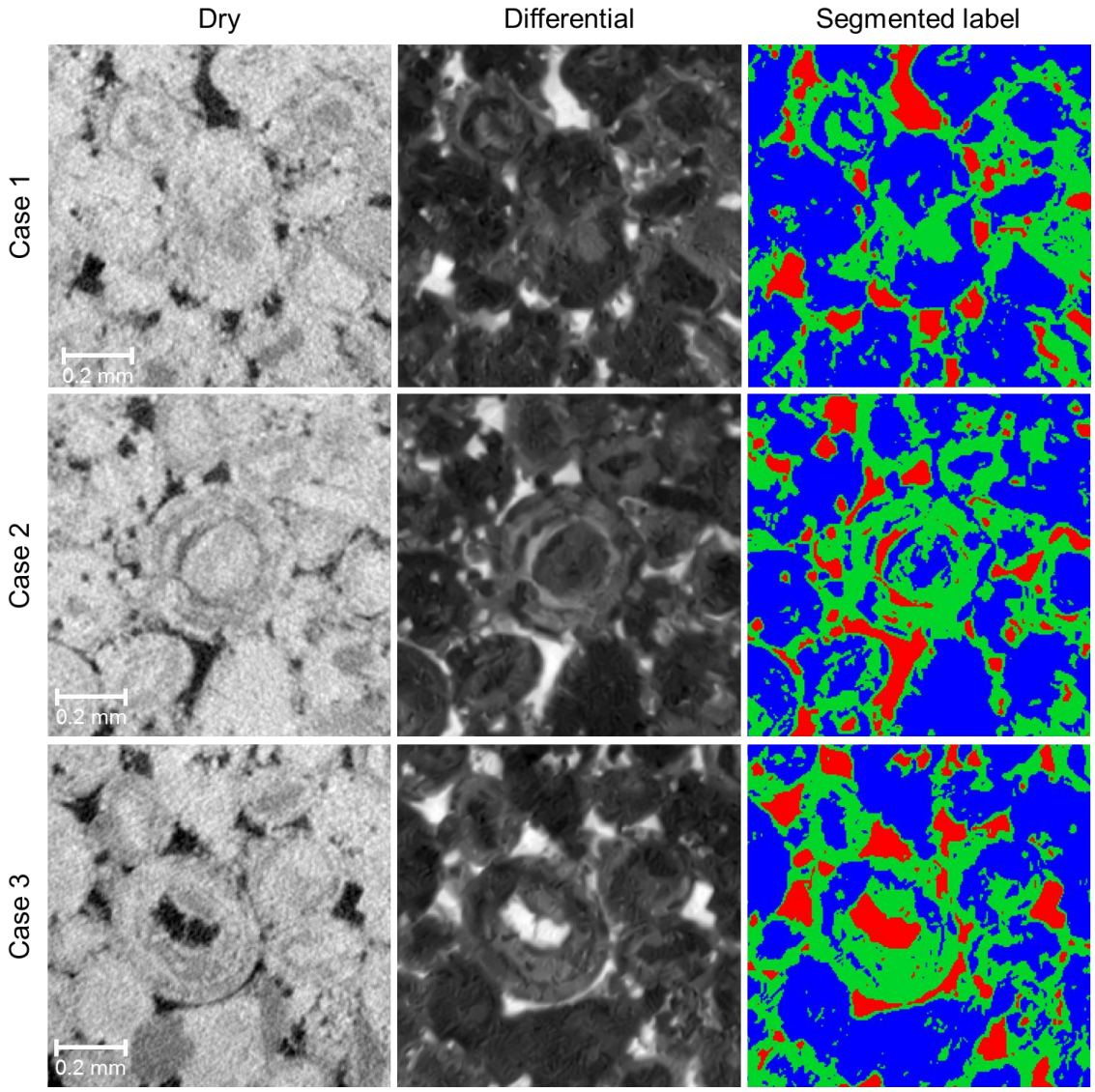

Figure 15. Three-phase dry, differential and segmented label images of 3 different regions of interest (Case 1, 2 and 3) in Portland showing how macro pores are connected through sub-resolution pores. The image dimensions are 200 x 200 pixels. Cases 1 and 2 show segmented label images illustrating how sub-resolution pores (green) may connect macro pores (red) situated between the grains (blue), while Case 3 illustrates a case where the sub-resolution pores connect the macro pores that exist closer to the grain centres. (For interpretation of the references to colour in this figure legend, the reader is referred to the web version of this article.)

After showing that sub-resolution pores can be identified and that the macro pores can be connected through these regions, we perform a further step to provide a better spatial description of sub-resolution porosity. We assume that the sub-resolution pores are characterised by a distribution represented by average porosity values $\tilde{\phi}$ for each sub-phase. In order to quantify this distribution, the histogram of the segmented sub-resolution pore phase (Figure 8e for Portland

and Figure 9e for Estaillades) is equally divided into five sub-regions depending on the grey-scale value, as shown in Figure 16.

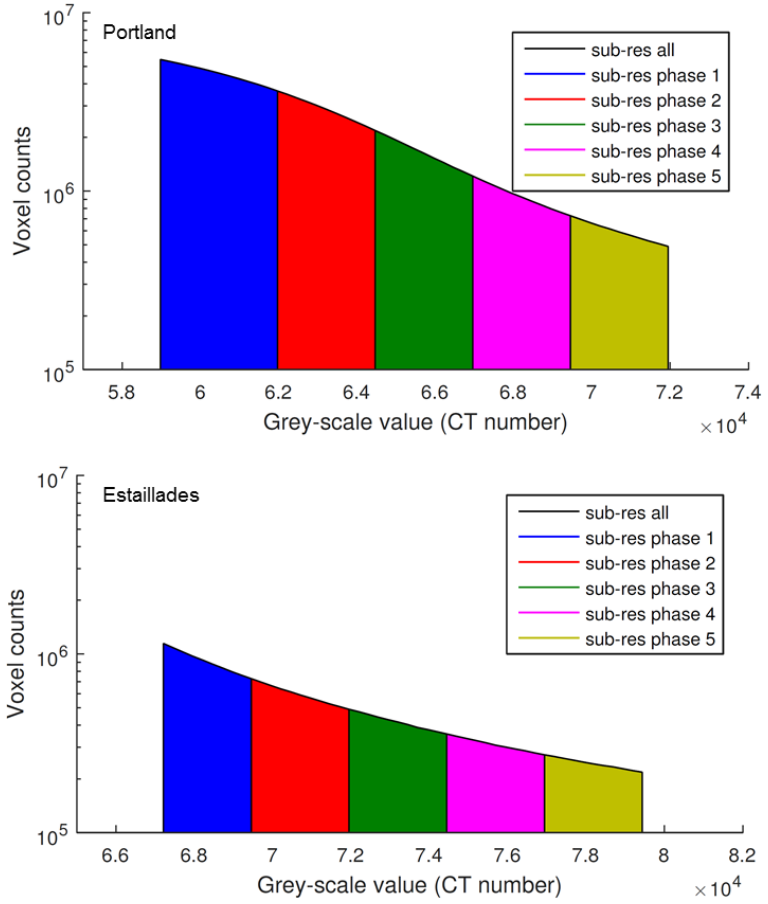

Figure 16. Equally dividing sub-resolution pores into five categories based on grey-scale values. Each colour represents one phase within the sub-resolution pore phase.

The new segmented label images containing these sub-regions with the corresponding average porosity values ($\tilde{\phi}$) can then be generated, as shown in Figure 17. The histogram plots for each sub-region are obtained by using the same method when generating Figure 13, as shown in Figure 18.

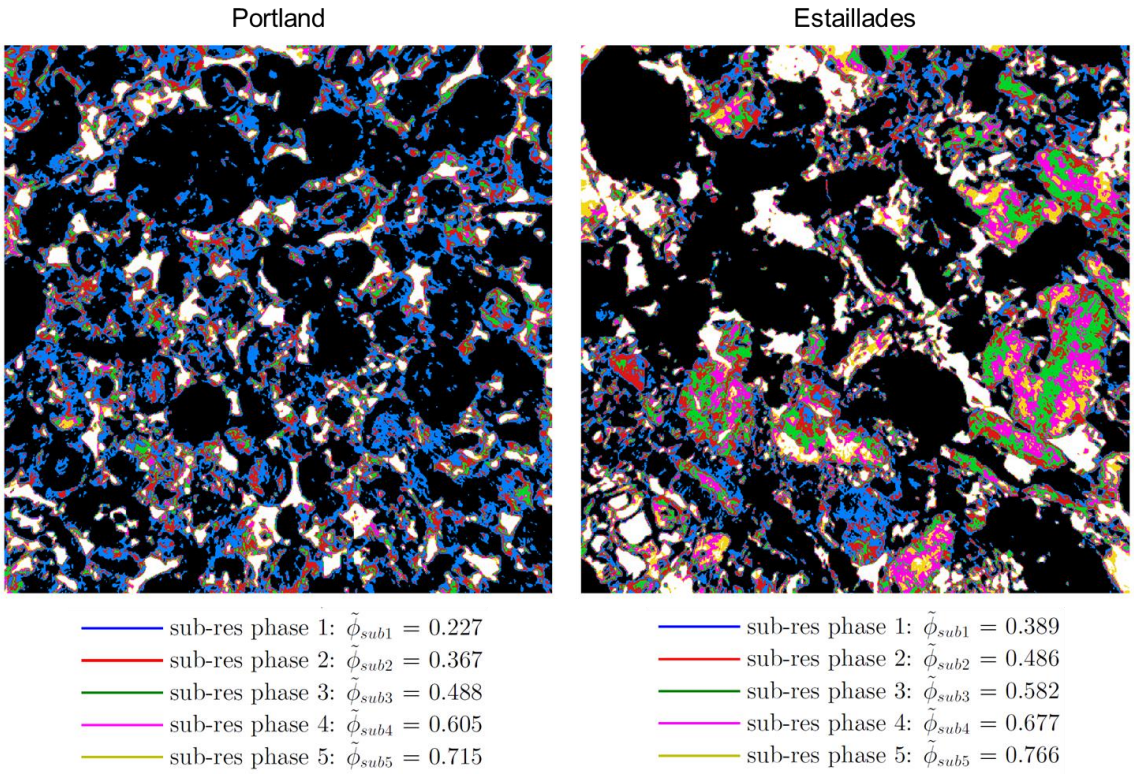

Figure 17. Segmented label images for Portland and Estaillades. The solid grain phase is shown in black and macro pore phase is shown in white. The sub-resolution pore phase is divided into five sub-regions with different $\tilde{\phi}$ values.

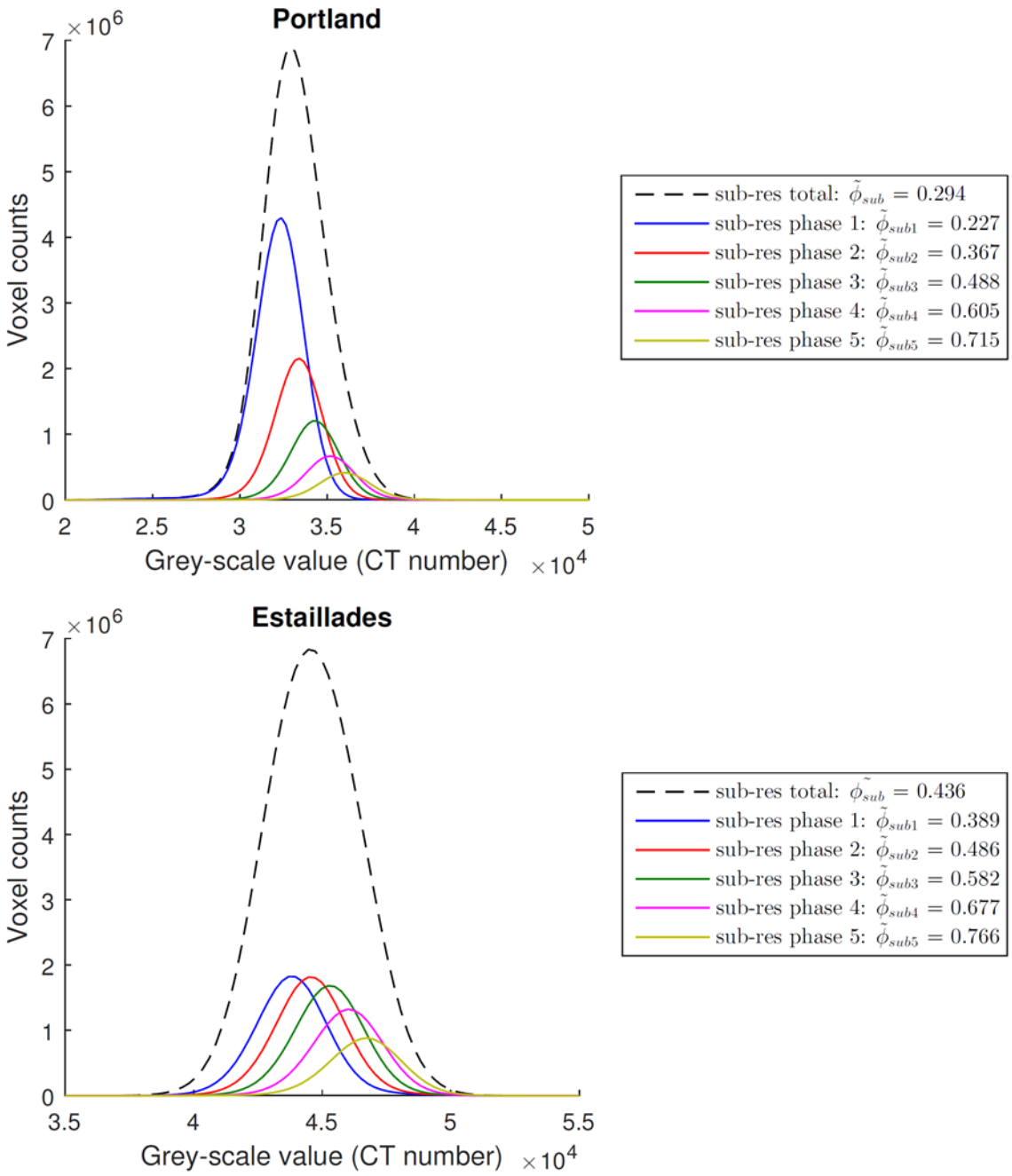

Figure 18. The histogram plot showing sub-resolution pores containing five sub-regions. The $\tilde{\phi}$ values for each sub-regions are calculated, which can be assigned to the segmented label images in Figure 17.

The values for average porosities associated with each sub-region vary from 0.227 to 0.715 for Portland and 0.389 to 0.766 for Estaillades. Each voxel in the sub-resolution porosity is now associated with one of the average porosity values for sub-regions. Using these values the total porosities calculated from contribution by macro pores and sub-resolution pores are 0.205 and 0.308 for Portland and Estaillades respectively – these values are slightly higher than the measurements from having a single sub-resolution pore phase but still agree well with Helium porosity measurements (see Table 1). This demonstrates the capability of the presented method to non-intrusively provide spatially resolved maps of sub-resolution porosity values.

4. Conclusions

We provide an X-ray tomography based experimental and image analysis methodology to non-invasively characterise sub-resolution porosity and connectivity of porous media with complex pore structure. We demonstrated our methodology through characterisation of porosity in two carbonate rocks. A procedure based on using high-salinity brine as contrast phase and applying differential imaging between the scans of porous samples saturated with a 30 wt% KI brine solution and dry scans is provided to obtain spatially-resolved maps of solid grain, sub-resolution and above-resolution (macro pores) voxels. The total porosity values from three phase segmentation for Portland and Estaillades carbonates are shown to be in good agreement with Helium porosity measurements.

The main advantage of using high-salinity brine as contract phase and capturing sub-resolution pore space in flow experiments is that it can identify low density minerals which have similar grey-scale values as sub-resolution pores. This is one of the main limitations when try to segment sub-resolution pores from dry scan images only. Moreover, the actual porosity values within the sub-resolution pores can be quantified. Additional advantages of the proposed flow-based experimental methodology are that the connectivity of the pores can be accurately estimated and further characterised through a distribution of porosity within the sub-resolution pores. This methodology serves as a basis for a detailed description of complex pore space that can be used for more quantitative future studies of flow and transport.

Acknowledgements

We gratefully acknowledge funding from DEA Deutsche Erdoel AG. We also acknowledge the Qatar Carbonates and Carbon Storage Research Centre (QCCSRC) for the access to the XMT facilities. B.B. and M.J.B. wish to thank the Engineering and Physical Science Research Council for the financial support through grant EP/L012227/1.

References

[1] Fredd CN, HS Fogler. Influence of transport and reaction on wormhole formation in porous media. AIChE Journal. 44 (1998) 1933-49, doi: 10.1002/aic.690440902.

[2] Gaus I, P Audigane, L André, J Lions, N Jacquemet, P Durst, I Czernichowski-Lauriol, M Azaroual. Geochemical and solute transport modelling for CO2 storage, what to expect from it? International Journal of Greenhouse Gas Control. 2 (2008) 605-25, doi: http://dx.doi.org/10.1016/j.ijggc.2008.02.011.

[3] Gelhar LW, C Welty, KR Rehfeldt. A critical review of data on field-scale dispersion in aquifers. Water Resources Research. 28 (1992) 1955-74, doi: 10.1029/92WR00607.

[4] Sayers CM. The elastic properties of carbonates. The Leading Edge. 27 (2008) 1020-4.

[5] Bijeljic B, P Mostaghimi, MJ Blunt. Insights into non-Fickian solute transport in carbonates. Water Resources Research. 49 (2013) 2714-28, doi: 10.1002/wrcr.20238.

[6] Norouzi Apourvari S, CH Arns. Image-based relative permeability upscaling from the pore scale. Advances in Water Resources. (2015), doi: http://dx.doi.org/10.1016/j.advwatres.2015.11.005.

[7] Cantrell DL, RM Hagerty. Microporosity in Arab Formation Carbonates, Saudi Arabia. GeoArabia. 4 (1999) 129-54.

[8] Moctezuma-Berthier A, O Vizika, JF Thovert, PM Adler. One- and Two-Phase Permeabilities of Vugular Porous Media. Transport in Porous Media. 56 (2004) 225-44, doi: 10.1023/B:TIPM.0000021843.08695.23.

[9] Gjetvaj F, A Russian, P Gouze, M Dentz. Dual control of flow field heterogeneity and immobile porosity on non-Fickian transport in Berea sandstone. Water Resources Research. 51 (2015) 8273-93, doi: 10.1002/2015WR017645.

[10] Scheibe TD, WA Perkins, MC Richmond, MI McKinley, PDJ Romero-Gomez, M Oostrom, TW Wietsma, JA Serkowski, JM Zachara. Pore-scale and multiscale numerical simulation of flow and transport in a laboratory-scale column. Water Resources Research. 51 (2015) 1023-35, doi: 10.1002/2014WR015959.

[11] Anovitz LM, DR Cole. Characterization and Analysis of Porosity and Pore Structures. Reviews in Mineralogy and Geochemistry. 80 (2015) 61-164.

[12] Ketcham RA, WD Carlson. Acquisition, optimization and interpretation of X-ray computed tomographic imagery: applications to the geosciences. Computers & Geosciences. 27 (2001) 381-400, doi: 10.1016/s0098-3004(00)00116-3.

[13] Lin Q, SJ Neethling, KJ Dobson, L Courtois, PD Lee. Quantifying and minimising systematic and random errors in X-ray micro-tomography based volume measurements. Computers & Geosciences. 77 (2015) 1-7, doi: http://dx.doi.org/10.1016/j.cageo.2014.12.008.

[14] Cnudde V, MN Boone. High-resolution X-ray computed tomography in geosciences: A review of the current technology and applications. Earth-Science Reviews. 123 (2013) 1-17, doi: http://dx.doi.org/10.1016/j.earscirev.2013.04.003.

[15] Lin Q, DJ Barker, KJ Dobson, PD Lee, SJ Neethling. Modelling particle scale leach kinetics based on X-ray computed micro-tomography images. Hydrometallurgy. 162 (2016) 25-36, doi: http://dx.doi.org/10.1016/j.hydromet.2016.02.008.

[16] Dhawan N, MS Safarzadeh, JD Miller, MS Moats, RK Rajamani, C-L Lin. Recent advances in the application of X-ray computed tomography in the analysis of heap leaching systems. Minerals Engineering. 35 (2012) 75-86, doi: http://dx.doi.org/10.1016/j.mineng.2012.03.033.

[17] Lai P, K Moulton, S Krevor. Pore-scale heterogeneity in the mineral distribution and reactive surface area of porous rocks. Chemical Geology. 411 (2015) 260-73, doi: http://dx.doi.org/10.1016/j.chemgeo.2015.07.010.

[18] Lin Q, SJ Neethling, L Courtois, KJ Dobson, PD Lee. Multi-scale quantification of leaching performance using X-ray tomography. Hydrometallurgy. 164 (2016) 265-77, doi: http://dx.doi.org/10.1016/j.hydromet.2016.06.020.

[19] Andrew M, B Bijeljic, MJ Blunt. Pore-scale imaging of trapped supercritical carbon dioxide in sandstones and carbonates. International Journal of Greenhouse Gas Control. 22 (2014) 1-14, doi: 10.1016/j.ijggc.2013.12.018.

[20] Menke HP, B Bijeljic, MG Andrew, MJ Blunt. Dynamic Three-Dimensional Pore-Scale Imaging of Reaction in a Carbonate at Reservoir Conditions. Environmental Science & Technology. 49 (2015) 4407-14, doi: 10.1021/es505789f.

[21] Iglauer S, MA Fernø, P Shearing, MJ Blunt. Comparison of residual oil cluster size distribution, morphology and saturation in oil-wet and water-wet sandstone. Journal of Colloid and Interface Science. 375 (2012) 187-92, doi: 10.1016/j.jcis.2012.02.025.

[22] Iassonov P, T Gebrenegus, M Tuller. Segmentation of X-ray computed tomography images of porous materials: A crucial step for characterization and quantitative analysis of pore structures. Water Resources Research. 45 (2009), doi: 10.1029/2009WR008087.

[23] Schlüter S, A Sheppard, K Brown, D Wildenschild. Image processing of multiphase images obtained via X-ray microtomography: A review. Water Resources Research. 50 (2014) 3615-39, doi: 10.1002/2014WR015256.

[24] Carroll S, Y Hao, M Smith, Y Sholokhova. Development of scaling parameters to describe CO2–rock interactions within Weyburn-Midale carbonate flow units. International Journal of Greenhouse Gas Control. 16, Supplement 1 (2013) S185-S93, doi: http://dx.doi.org/10.1016/j.ijggc.2012.12.026.

[25] Mangane PO, P Gouze, L Luquot. Permeability impairment of a limestone reservoir triggered by heterogeneous dissolution and particles migration during CO2-rich injection. Geophysical Research Letters. 40 (2013) 4614-9, doi: 10.1002/grl.50595.

[26] Qajar J, CH Arns. Characterization of reactive flow-induced evolution of carbonate rocks using digital core analysis- part 1: Assessment of pore-scale mineral dissolution and deposition. Journal of Contaminant Hydrology. 192 (2016) 60-86, doi: http://dx.doi.org/10.1016/j.jconhyd.2016.06.005.

[27] Garing C, P Gouze, M Kassab, M Riva, A Guadagnini. Anti-correlated Porosity–Permeability Changes During the Dissolution of Carbonate Rocks: Experimental Evidences and Modeling. Transport in Porous Media. 107 (2015) 595-621, doi: 10.1007/s11242-015-0456-2.

[28] Peters CA. Accessibilities of reactive minerals in consolidated sedimentary rock: An imaging study of three sandstones. Chemical Geology. 265 (2009) 198-208, doi: http://dx.doi.org/10.1016/j.chemgeo.2008.11.014.

[29] Smith MM, Y Sholokhova, Y Hao, SA Carroll. CO2-induced dissolution of low permeability carbonates. Part I: Characterization and experiments. Advances in Water Resources. 62, Part C (2013) 370-87, doi: http://dx.doi.org/10.1016/j.advwatres.2013.09.008.

[30] Bauer D, S Youssef, M Fleury, S Bekri, E Rosenberg, O Vizika. Improving the Estimations of Petrophysical Transport Behavior of Carbonate Rocks Using a Dual Pore Network Approach Combined with Computed Microtomography. Transport in Porous Media. 94 (2012) 505-24, doi: 10.1007/s11242-012-9941-z.

[31] Bultreys T, L Van Hoorebeke, V Cnudde. Multi-scale, micro-computed tomography-based pore network models to simulate drainage in heterogeneous rocks. Advances in Water Resources. 78 (2015) 36-49, doi: http://dx.doi.org/10.1016/j.advwatres.2015.02.003.

[32] Garing C, L Luquot, PA Pezard, P Gouze. Electrical and flow properties of highly heterogeneous carbonate rocks. AAPG Bulletin. 98 (2014) 49-66.

[33] Soulaine C, F Gjetvaj, C Garing, S Roman, A Russian, P Gouze, HA Tchelepi. The Impact of Sub-Resolution Porosity of X-ray Microtomography Images on the Permeability. Transport in Porous Media. 113 (2016) 227-43, doi: 10.1007/s11242-016-0690-2.

[34] Luquot L, O Rodriguez, P Gouze. Experimental Characterization of Porosity Structure and Transport Property Changes in Limestone Undergoing Different Dissolution Regimes. Transport in Porous Media. 101 (2014) 507-32, doi: 10.1007/s11242-013-0257-4.

[35] Freire-Gormaly M, JS Ellis, A Bazylak, HL MacLean. Comparing thresholding techniques for quantifying the dual porosity of Indiana Limestone and Pink Dolomite. Microporous and Mesoporous Materials. 207 (2015) 84-9, doi: http://dx.doi.org/10.1016/j.micromeso.2015.01.002.

[36] Boone MA, T De Kock, T Bultreys, G De Schutter, P Vontobel, L Van Hoorebeke, V Cnudde. 3D mapping of water in oolithic limestone at atmospheric and vacuum saturation using X-ray micro-CT differential imaging. Materials Characterization. 97 (2014) 150-60, doi: http://dx.doi.org/10.1016/j.matchar.2014.09.010.

[37] Ghous A, TJ Senden, RM Sok, AP Sheppard, VW Pinczewski, MA Knackstedt. 3D Characterisation of Microporosity in Carbonate Cores. Society of Petrophysicists and Well-Log Analysts. (2007).

[38] Latham S, T Varslot, A Sheppard. Image registration: enhancing and calibrating X-ray micro-CT imaging. Proc of the Soc Core Analysts, Abu Dhabi, UAE. (2008).

[39] Bhattad P, B Young, CF Berg, AB Rustad, O Lopez. X-RAY MICRO-CT ASSISTED DRAINAGE ROCK TYPING FOR CHARACTERIZATION OF FLOW BEHAVIOUR OF LAMINATED SANDSTONE RESERVOIRS. e International Symposium of the Society of Core Analysts held in Avignon, France2014.

[40] Pini R. Multidimensional Quantitative Imaging of Gas Adsorption in Nanoporous Solids. Langmuir. 30 (2014) 10984-9, doi: 10.1021/la502582c.

[41] Alyafei N, MJ Blunt. The effect of wettability on capillary trapping in carbonates. Advances in Water Resources. In press (2016), doi: http://dx.doi.org/10.1016/j.advwatres.2016.02.001.

[42] Buades A, B Coll, J-M Morel. Nonlocal Image and Movie Denoising. International Journal of Computer Vision. 76 (2008) 123-39, doi: 10.1007/s11263-007-0052-1.

[43] Otsu N. A threshold selection method from gray-level histograms. IEEE Transactions on Systems, Man and Cybernetics. 9 (1979) 62-6, doi: citeulike-article-id:1116982.

[44] Liao P, T Chen, P Chung. A fast algorithm for multilevel thresholding. Journal of Information Science and Engineering. 17 (2001) 713-27.

[45] Jones AC, CH Arns, AP Sheppard, DW Hutmacher, BK Milthorpe, MA Knackstedt. Assessment of bone ingrowth into porous biomaterials using MICRO-CT. Biomaterials. 28 (2007) 2491-504, doi: http://dx.doi.org/10.1016/j.biomaterials.2007.01.046.

[46] Vincent L, L Vincent, P Soille. Watersheds in Digital Spaces: An Efficient Algorithm Based on Immersion Simulations. IEEE Transactions on Pattern Analysis and Machine Intelligence. 13 (1991) 583-98, doi: 10.1109/34.87344.